10-22-2019

Samarium-Activated La2Hf2O7 Nanoparticles as Multifunctional Phosphors

Santosh K. Gupta
The University of Texas Rio Grande Valley

Maya Abdou
The University of Texas Rio Grande Valley

Jose P. Zuniga
The University of Texas Rio Grande Valley

Alexander A. Puretzky

Yuanbing Mao
The University of Texas Rio Grande Valley

Recommended Citation

Gupta, S. K., Abdou, M., Zuniga, J. P., Puretzky, A. A., & Mao, Y. (2019). Samarium-Activated La2Hf2O7 Nanoparticles as Multifunctional Phosphors. ACS Omega, 4(19), 17956–17966. https://doi.org/10.1021/acsomega.9b01318

ACS OMEGA

Article

Cite This: ACS Omega 2019, 4, 17956−17966

http://pubs.acs.org/journal/acsodf

Samarium-Activated $La_2Hf_2O_7$ Nanoparticles as Multifunctional Phosphors

Santosh K. Gupta,[†,‡] Maya Abdou,[†] Jose P. Zuniga,[†] Alexander A. Puretzky,[§] and Yuanbing Mao*[,†,∥,⊥]

[†]Department of Chemistry and [∥]School of Earth, Environmental, and Marine Sciences, University of Texas Rio Grande Valley, 1201 West University Drive, Edinburg, Texas 78539, United States

[‡]Radiochemistry Division, Bhabha Atomic Research Centre, Trombay, Mumbai 400085, India

[§]Center for Nanophase Materials Sciences, Oak Ridge National Laboratory, Oak Ridge, Tennessee 37831, United States

Supporting Information

ABSTRACT: Recent developments in the field of designing novel nanostructures with various functionalities have pushed the scientific world to design and develop high-quality nanomaterials with multifunctional applications. Here, we propose a new kind of doped metal oxide pyrochlore nanostructure for solid-state phosphor, X-ray scintillator, and optical thermometry. The developed samarium-activated $La_2Hf_2O_7$ (LHOS) nanoparticles (NPs) emit a narrow and stable red emission with lower color temperature and adequate critical distance under near-UV and X-ray excitations. When the LHOS NPs are exposed to an energetic X-ray beam, the Sm^{3+} ions situated at the symmetric environment get excited along with those located at the asymmetric environment, which results in a low asymmetry ratio of Sm^{3+} under radioluminescence compared to photoluminescence. High activation energy and adequate thermal sensitivity of the LHOS NPs highlight their potential as a thermal sensor. Our results indicate that these Sm^{3+}-activated $La_2Hf_2O_7$ NPs can serve as a multifunctional UV, X-ray, and thermographic phosphor.

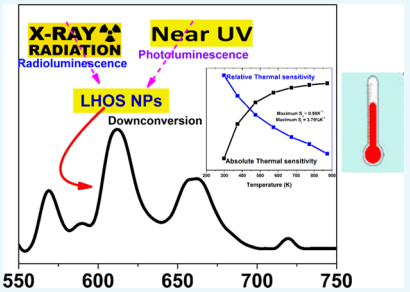

1. INTRODUCTION

In the current era of materials science, new kinds of functional materials have been continuously developed to reduce the burden from increasing human demand in the areas of energy, health, environment, food security, agriculture, and so forth.[1−5] Some materials which can perform multiple functions in a system because of their unique properties are known as multifunctional materials. Such materials can reduce human workload and improve our lifestyle by virtue of their efficiency, reliability, cost-efficiency, and scalability. In the areas of photonics and optoelectronics, a phosphor material which can function for solid-state lighting, scintillation, and luminescence thermometer is desirable for meeting a multitude of demands. Phosphor materials synthesized in a nanodomain offer a high electron−hole overlap integral, large light collection, and ease of coating on films/fibers.[6,7] The host-to-dopant energy-transfer process in nanosized phosphors is highly relevant because of their potential to exhibit higher-resolution displays at lower thermal budget relative to their bulk counterparts.[8] Lanthanide ion-doped nanoparticles (NPs) have displayed outstanding photophysical properties such as large Stoke shift, high color purity, higher excited-state lifetime, and substantial quantum efficiency.[7,9] Such unique properties provide obvious advantages for luminescent materials designed toward UV-excited phosphors, X-ray scintillators, and thermographic phosphors (TGPs). Designing efficient nanosized phosphors which display all these application potentials would help solve a variety of issues in the areas of optical technology. This study is intended to meet these challenges and fill the gap.

UV-based and blue light phosphors are used for solid-state lighting, light-emitting diodes, display panels, sensors, biomedical imaging and diagnostics, catalysts, and so forth.[10,11] Their application in white light-emitting diodes is in high demand because of their desirable power output, longevity, environment benignness, and low cost.[12] However, the present commercial white light lamps through a combination of a yellow phosphor ($YAG:Ce^{3+}$) and a blue light-emitting diode chip (InGaN) suffer from low color rendering index and high correlated color temperature (CCT) problems because of the lack of suitable red components.[13,14] Therefore, continuous search for better red phosphors with low CCT, high color purity, and high structural and thermal stability is undergoing.

Scintillators are in high demand because of their broad applications for ionizing radiation detectors, X-ray imaging, biological and medical diagnostics, photodynamic therapy, and so forth.[15,16] Their single crystal or bulk form suffers from difficult optical property tuning, long processing time, sophisticated instrumentation, and high fabrication cost.[15] NPs and nanoceramics are expected to meet these challenges because of the dominance of surface atoms with strains and

Received: May 7, 2019
Accepted: October 7, 2019
Published: October 22, 2019

DOI: 10.1021/acsomega.9b01318
ACS Omega 2019, 4, 17956−17966

electron−hole overlap integral to fine-tune their optical properties.

Moreover, phosphors have been explored for thermal sensing as TGPs because of their temperature-dependent photoluminescence (PL) characteristics such as emission intensity and excited-state lifetime. As luminescence thermometers, TGPs have obvious advantages over other conventional thermal sensing methods as they do not require direct contact, are operational in harsh conditions where large electromagnetic noises exist, and work well in aqueous systems. They also have fast response and high sensitivity and accuracy. Lanthanide-doped materials, such as silicates, garnets, and niobates, have gained significant momentum for such application because of their high spatial resolution and accuracy of temperature gradients.[17] Most of the relevant work has been performed in the visible region of electromagnetic spectrum to determine the temperature of running jet turbines, gas centrifuges, and chemical reaction vessels.[18] However, current TGPs are restricted to bulk samples with moderate sensitivity and intermediate temperature range.

$La_2Hf_2O_7$ (LHO) is a desirable host for efficient lanthanide-doped phosphor materials because of its high structural stability, wide band gap, the ability to accommodate dopant ions at both La^{3+} and Hf^{4+} sites, and high radiation stability, refractive index, and dielectric constant.[19] $Y_2Ti_2O_7$ pyrochlore has a phonon frequency <712 cm^{-1}, which is expected to decrease for heavier hafnate-based pyrochlores.[20] As a result, LHO could have low nonradiative relaxations and accordingly enhanced luminescence intensity. It also has high stopping power for X- and γ-rays because of its high density of 7.9 g/cm^3 and the presence of hafnium with atomic number 72. Sm^{3+}-doped phosphors exhibit sharp emission bands and long excited-state lifetimes, and the large difference between the lowest luminescent level and the highest nonluminescent level of Sm^{3+} ions makes it an excellent structural probe.[21] To the best of our knowledge, there is no report on designing multifunctional nanosized phosphors using Sm^{3+}-doped LHO (LHOS) NPs as UV, X-ray, and TGPs.

In this paper, we report the exploration of our LHOS NPs synthesized by a molten salt synthesis (MSS) method as a new type of multifunctional UV-excited phosphor, X-ray scintillator, and TGP. Under near-UV excitation, these NPs demonstrate red emission and 2.5% quenching concentration. Magnetic dipole transition (MDT) at ∼568 nm is absent, which suggests a highly asymmetric environment of Sm^{3+} ions in the LHO lattice and endows high red color purity. Under X-ray irradiation, these NPs show orange-red emission with the presence of intense MDT peak. The LHOS NPs also display favorable thermal stability and good photo-/radioluminescence efficiencies. The high activation energy and desirable thermal sensitivity for luminescence thermometer are attributed to the low phonon energy, low defect density, high crystal quality, and high structural stability of the LHO host. Overall, our LHOS NPs demonstrate multifunctional application potentials as UV, X-ray, and TGPs.

2. RESULTS AND DISCUSSION

2.1. Phase, Crystallite Size, and Morphology of the LHOS NPs. The synthesized LHOS NPs are in the ideal pyrochlore phase with $Fd\bar{3}m$ space group (Figure S2) and are nanospheres with particle size between 20 and 70 nm (Figure S3) as investigated by X-ray diffraction (XRD) and scanning electron microscopy (SEM), respectively.

2.2. Structural Analysis: Raman and FTIR Spectroscopy. On the basis of the concepts of group theory, the Raman spectra of ideal pyrochlore $A_2B_2O_7$ compounds ($Fd\bar{3}m$ space group) consist of six well-defined and sharp vibrational peaks in the range 200−1000 cm^{-1}, which are ascribed to A_{1g} + E_g + $4F_{2g}$.[22,23] Radius ratio (r_A/r_B) plays an important role to decide the exact structure of $A_2B_2O_7$ compounds. When r_A/r_B > 1.46, an ordered pyrochlore is the most prevalent structure.[24] LHO prefers to stabilize in an ideal pyrochlore structure because r_{La} (CN = 8) = 1.16 Å and r_{Hf} (CN = 6) = 0.710 Å, giving $r_{La^{3+}}/r_{Hf^{4+}}$ = 1.63. Figure 1a shows the Raman spectra of the LHOS NPs that exhibit peaks located approximately at 306, 320, 397, 498, 519, and 615 cm^{-1} (see deconvoluted spectra in Figure 1b), which correspond to F_{2g}, E_g, F_{2g}, A_{1g}, F_{2g}, and F_{2g} modes.[25] Specifically, the peaks at 306, 320, and 397 cm^{-1} are originated from the vibrations of the metal−oxygen bonds (i.e., La−O and Hf−O bonds). The 519 and 615 cm^{-1} peaks arise from the Hf−O stretching. The 498 cm^{-1} peak arising from the A_{1g} mode is attributed to the bending of O−Hf−O bond in HfO_6 octahedra.[26] The small peak at around 769 cm^{-1} is ascribed to the distortion of the HfO_6 octahedra.[27] Therefore, based on our Raman data, the LHOS NPs have the ideal pyrochlore structure. Moreover, changing of Sm^{3+} doping concentration (≤10%) does not distort the basic pyrochlore matrix of the LHO host, as can be seen from the Raman spectra.

In the Fourier transform infrared (FTIR) spectra of the LHOS NPs (Figure 1c), the broad-band peaks located at around 3400 cm^{-1} are attributed to stretching of surface-adsorbed water molecules on the LHOS NPs.[28] The peaks at around 1330−1500 cm^{-1} are due to bending vibration of OH bond.[29] The IR bands at around 840−920 cm^{-1} are attributed to wagging vibration of NH band, which may come from the used NH_4OH during the coprecipitation process. The IR peaks at around 510 cm^{-1} are the absorption bands characteristic to pyrochlore $A_2Hf_2O_7$ compounds, which is consistent with the Raman data shown above.[30] The expanded FTIR spectra in the low wavelength range clearly depict the characteristic absorption of rare earth hafnates (Figure 1d). The absorption bands characteristic of $A_2B_2O_7$ hafnates pyrochlore structure was reported by Klee and Weitz.[31] In fact, Sevastyanov and group[30] have observed absorption from $Nd_2Hf_2O_7$ and $Gd_2Hf_2O_7$ pyrochlore at around 530−540 cm^{-1}.

2.3. PL Spectroscopy. The PL excitation spectra of the LHOS NPs recorded at 607 nm corresponding to the $^4G_{5/2} \rightarrow {}^6H_{5/2}$ emission of Sm^{3+} (Figure 2a) can be divided into two regions. The first region with a very weak band at around 275−300 nm is attributed to the charge transfer from $O^{2-} \rightarrow Sm^{3+}$ ion. The second region from 300 to 500 nm of the excitation spectra includes fine peaks at 322, 345, 362, 377, 405, 420, 446, 461, 467, 472, 480, and 490 nm, which correspond to the transitions of Sm^{3+} ions: $^6H_{5/2} \rightarrow {}^2L_{15/2}$, $^6H_{5/2} \rightarrow {}^4H_{9/2}$, $^6H_{5/2} \rightarrow {}^4D_{3/2}$, $^6H_{5/2} \rightarrow {}^4D_{1/2}$, $^6H_{5/2} \rightarrow {}^4F_{7/2}$, $^6H_{5/2} \rightarrow {}^4P_{5/2}$, $^6H_{5/2} \rightarrow {}^4G_{9/2}$, $^6H_{5/2} \rightarrow {}^4I_{9/2}$, $^6H_{5/2} \rightarrow {}^4I_{11/2}$, $^6H_{5/2} \rightarrow {}^4I_{13/2}$, and $^6H_{5/2} \rightarrow {}^4I_{15/2}$, respectively.[32] More interestingly, the Laporte forbidden f−f excitation bands of the LHOS NPs are found to be more intense than the charge-transfer band. This phenomenon indicates that the LHO host has low phonon energy and the energy levels of the doped Sm^{3+} ions match well with the band structure of LHO for broad phosphor applications. It is supplemented by lower phonon energy of the LHO host (745 cm^{-1}) together with relaxation of f−f

DOI: 10.1021/acsomega.9b01318
ACS Omega 2019, 4, 17956−17966

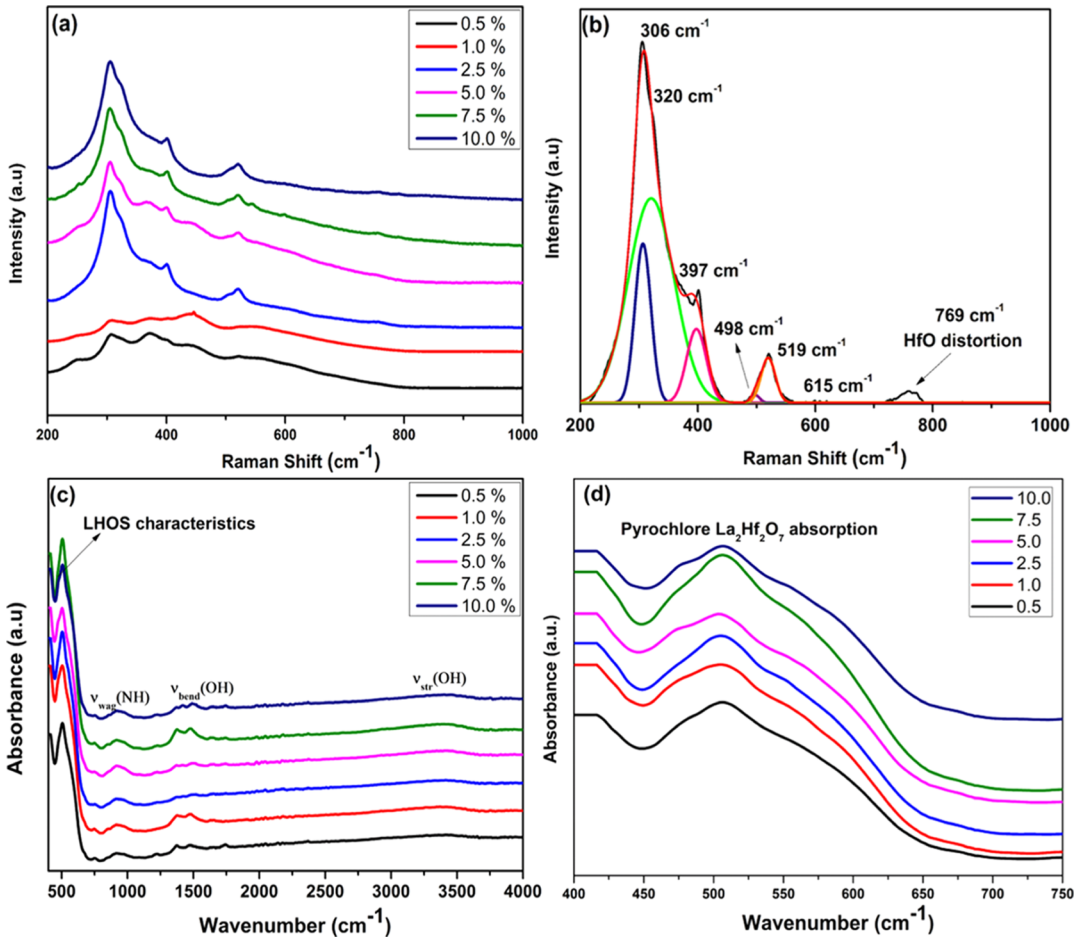

Figure 1. (a) Raman spectra and (b) vibrational peak characteristics of ideal pyrochlore structure obtained after Gaussian fitting, (c) FTIR spectra, and (d) expanded FTIR spectra at low wavenumbers of the LHOS NPs.

transition in the presence of a crystalline field offered by the LHO host.

The three main PL emission peaks of the LHOS NPs under 405 nm excitation are at 605, 653, and 717 nm (Figure 2b), corresponding to the $^4G_{5/2} \rightarrow {}^6H_{7/2}$, $^4G_{5/2} \rightarrow {}^6H_{9/2}$, and $^4G_{5/2} \rightarrow {}^6H_{11/2}$ transitions of Sm^{3+} ions.[33] Intriguingly, the MDT $^4G_{5/2} \rightarrow {}^6H_{5/2}$ at ∼565 nm is absent, indicating that the majority of Sm^{3+} ions are located at sites without inversion center. The $A_2B_2O_7$-type ordered pyrochlore structure of the $La_2Hf_2O_7$ host with LaO_8 and HfO_6 coordinations is depicted in Figure S4a.[34] Samarium ions are expected to occupy both La and Hf sites, which is also shown pictorially in Figure S4b. On the basis of ionic size and charge, a large fraction of samarium ions is localized at distorted LaO_8 scalenohedra.

In our case, they are localized at highly asymmetric sites in the LHO host. This phenomenon is consistent with (i) the large spectral splitting of the $^4G_{5/2} \rightarrow {}^6H_{7/2}$, $^4G_{5/2} \rightarrow {}^6H_{9/2}$, and $^4G_{5/2} \rightarrow {}^6H_{11/2}$ transitions observed (Figure 2b) and (ii) the high luminescence intensity of the 653 nm peak corresponding to the electric dipole transition (EDT) $^4G_{5/2} \rightarrow {}^6H_{9/2}$. Moreover, the characteristic $^4G_{5/2} \rightarrow {}^6H_{7/2}$ transition of Sm^{3+} ions has mixed electric and magnetic dipoles, which contribute to the orange-red emission at 605 nm as the strongest peak.[35] Because there is no MDT emission and strong EDT at 653 nm, the asymmetry ratio value of the LHOS NPs is much higher than that of Eu^{3+}-doped $La_2Hf_2O_7$ NPs (∼3.0).[19,36] It is reported that surface defects and cation vacancies are deleterious to PL efficiency where oxygen vacancies may induce improved emissions by virtue of energy transfer.[37] Previously, we observed violet-blue emission from undoped LHO NPs under UV irradiation, which was attributed to the presence of ionized oxygen vacancies in the band gap of the undoped LHO NPs based on density functional theory calculations.[38] In one of our earlier work, we have estimated the band gap of LHO to be 5.63 eV using hybrid exchange−correlation functional (HSE06)[38] and is in close agreement with the experimental value of 5.6 ± 0.1 eV. LHO with a large band gap value of 5.6 eV can provide enough space to accommodate Sm^{3+} 4f energy levels and effectively reduce the probability of the overlapping between the lowest 4f state of Sm^{3+} ions and the conduction band maxima of the LHO host.[39] The energy transfer is mediated through ionized oxygen vacancies which are localized within the band gap of LHO and transfer photon energy to excited states of samarium ions. The energy levels of dopant Sm^{3+} ions are situated within the band gap of the LHO host. On the basis of our earlier report[38,40] and close similarity between Sm^{3+} and Eu^{3+}, Sm d- and f-states are present in both valence and conduction bands of LHO as both minority and majority spin components. This makes the interaction between O 2p states and Sm d/f states highly feasible to facilitate efficient host-to-dopant energy transfer. On the basis of the Dexter proposal, an effective energy transfer needs a good spectral overlap between the donor emission and the acceptor excitation.[41] To further

DOI: 10.1021/acsomega.9b01318
ACS Omega 2019, 4, 17956−17966

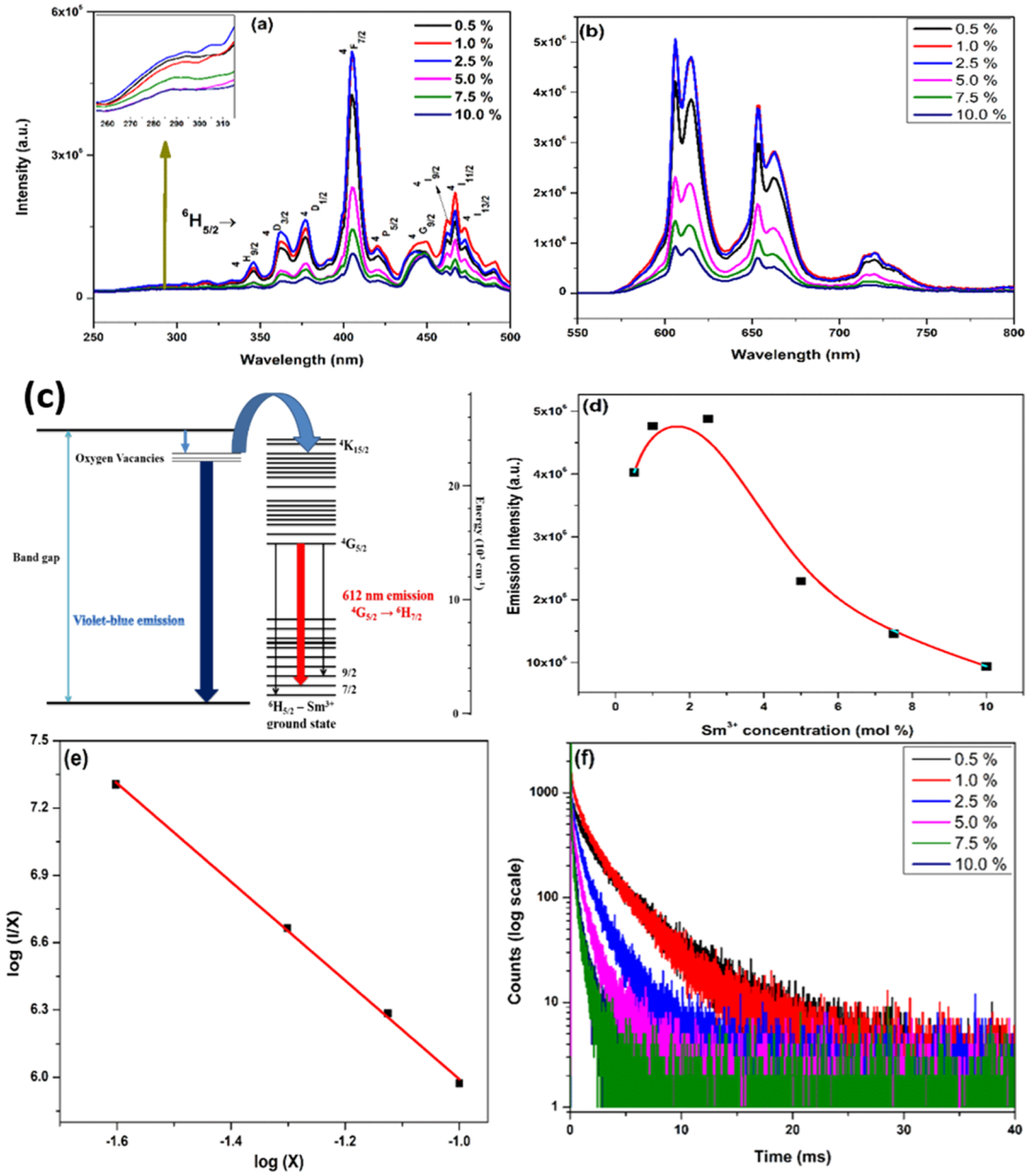

Figure 2. (a) PL excitation spectra (λ_{em} = 607 nm), (b) PL emission spectra (λ_{ex} = 405 nm), (c) proposed mechanism of host-to-dopant energy transfer, (d) variation of integrated emission intensity in the range of 575−675 nm as a function of Sm^{3+} doping concentration, (e) relation between $\log_{10}(I/x)$ and $\log_{10}(x)$ based on the Van Uitert equation, and (f) luminescence decay profiles of the LHOS NPs with Sm^{3+} doping level from 0.5 to 10.0%. The inset of Figure 1a shows the magnified excitation spectra in the wavelength range of 260−315 nm.

validate these results, we have shown experimental results on the spectral overlap between the emission of the LHO host (donor) and the excitation of Sm^{3+} ions (acceptor) (Figure S5a), which suggests an efficient energy transfer from the host to the dopant ions.

To study the role of oxygen vacancies on the PL spectra, both undoped LHO NPs and the LHOS NPs were annealed under an oxygen-deficient atmosphere and vacuum. Reducing atmosphere annealing was avoided to prevent reduction of Hf^{4+} ions in the samples.[33] The PL spectral results (Figure S5b) demonstrated that the vacuum annealing enhanced the violet-blue emission intensity for the undoped LHO compared to the initially prepared sample in air.[38] For the LHOS NPs, the red emission intensity increased to 2.5 times after vacuum annealing because of the increase of oxygen vacancy concentration. At the same time, the disappearance of the oxygen vacancy-related band at 400 nm from the LHO NPs to the LHOS NPs confirms the efficient energy transfer between the oxygen vacancy of the LHO host and Sm^{3+} dopant ions in the LHOS NPs.

2.4. Concentration Quenching Study. Dopant concentration plays important roles in the luminescence performance of phosphors. The Sm^{3+} doping level in the LHOS NPs changes their PL intensity but does not affect the spectral profile because of the strong shielding of 4f electrons of Sm^{3+} ions by the outer lying $5s^2$ and $5p^6$ electrons (Figure 2b).[42] The initial increase of PL emission intensity is ascribed to the increase of Sm^{3+} doping percentage; therefore, more luminophores are available for excitation by near-UV light at 405 nm. After 2.5 mol % doping level, the distance between Sm^{3+} ions decreases to an extent that there is enhanced probability of nonradiative energy transfer between adjacent

DOI: 10.1021/acsomega.9b01318
ACS Omega 2019, 4, 17956−17966

Sm^{3+} ions as concentration quenching. The quenching concentration of Sm^{3+} ions of these LHOS NPs is 2.5 mol % (Figure 2d), which is comparable with other reported Sm^{3+}-doped inorganic hosts in the literature (Table S2).

To understand the underlying nonradiative energy-transfer mechanism, that is, exchange interaction, radiation reabsorption, or multipole−multipole interaction, of these LHOS NPs, we turn to the empirical relationship proposed by Blasse to determine the critical distance (R_c) at which concentration quenching takes place based on eq S1.[43]

On average, there is one activator ion per V/X_cN. The calculated critical distance R_c of the LHOS (2.5 mol %) NPs is 30.9 Å, which is much larger than the typical critical distance responsible for energy transfer via exchange interaction (5 Å). Because radiation reabsorption is only effective when the emission spectrum of the donor and the excitation spectrum of the acceptor overlap broadly, which is not the case for the LHOS NPs, we can rule out the radiation reabsorption mechanism here. Therefore, electric multipole−multipole interaction would be the main mechanism responsible for the energy transfer from one Sm^{3+} ion to another in the LHOS NPs. It means that the Sm^{3+} ions localized at two LaO_8 scalenohedra at a distance less than 30.9 Å would undergo nonradiative energy transfer and leads to luminescence quenching by orbital overlap.

The calculated critical distance R_c of the LHOS NPs is larger compared to the reported values of other lanthanide-doped pyrochlores, such as $Nd_2Zr_2O_7$:Eu^{3+} (13.64 Å), $Y_2Ti_2O_7$:Eu^{3+} (6.47 Å), $Gd_2Zr_2O_7$:Sm^{3+} (6.28 Å), $La_2Ti_2O_7$:Er^{3+} (13.8 Å), $La_2Zr_2O_7$:Eu^{3+} (5.0 Å), and $CaYTiNbO_7$:Eu^{3+} (8.0 Å).[44−49] This can be attributed to the low phonon energy and nanocrystalline nature of the LHO host.

We have used the Van Uitert equation to confirm the multipole−multipole interaction as the exact nonradiative energy-transfer mechanisms for our LHOS NPs.[50] If nonradiative energy transfer involves the same acceptor and donor ions (i.e., Sm^{3+} in the case here), the type of electric multipolar interaction can be deciphered from the variation in emission intensity per unit concentration using the relation S2.

When $\theta = 3$, nonradiative energy transfer proceeds via exchange interaction, $\theta = 6$ corresponds to dipole−dipole (d−d) interaction, $\theta = 8$ corresponds to dipole−quadrupole (d−p) interaction, and $\theta = 10$ corresponds to quadrupole−quadrupole (q−q) interaction.[51] Applying the condition of $\beta(x)\theta/3 \gg 1$, eq S2 is simplified as eq S3.

The slope of this equation $(-\theta/3)$ obtained by plotting $\log(I/x)$ versus $\log(x)$ gives the electric multipolar characteristic value θ. For our LHOS NPs, the slope is −2.19814 (Figure 2e), so θ is approximately 6, corresponding to the dipole−dipole interaction, as similarly observed from $La_2Ti_2O_7$:Eu.[52]

2.5. Luminescence Lifetime Spectroscopy. Understanding local site occupancy is important to interpret the local symmetry around dopant ions in a host and optimize the luminescence properties of phosphors. Population analysis and number of lifetime components from lifetime spectra enable us to predict the local structure of dopant ions in hosts. The luminescence decay profiles of the LHOS NPs (Figure 2f) under excitation and emission wavelengths of 405 and 607 nm, respectively, can be fitted with a biexponential function using eq S4 with a time resolution of 1−2 μs.

In ordered pyrochlore LHO, La^{3+} ions exist in an eightfold coordination in highly distorted scalenohedra, whereas Hf^{4+} ions exist in a sixfold coordination in ideal octahedra, as confirmed by our XRD and Raman spectra data (Figures S2 and 1).[29] Both the lifetime values are attributed to Sm^{3+} ions localized at La^{3+} sites in distorted scalenohedra geometry. It is known that there is high concentration of defects in pyrochlore structure. If LaO_8 is surrounded by such defects, the LHOS NPs have more nonradiative channels and therefore short decay lifetime. Otherwise, defects are at long distance with long lifetime of the LHOS NPs.[53,54] Specifically, the long-lived component τ_2 is ascribed to Sm^{3+} ions occupying LaO_8 scalenohedra sites, which are at long distance from point or structural defects. On the other hand, the fast decaying component τ_1 is due to Sm^{3+} ions localized at LaO_8 scalenohedra but at proximity of defects. In addition, both the lifetime values of the LHOS NPs decrease monotonically with increasing Sm^{3+} doping concentration (Table S3). This can also be seen from the variations of the short- and long-lived lifetimes with Sm^{3+} concentration (Figure S6). This may be attributed to enhanced probability of nonradiative energy transfer among Sm^{3+} ions with increasing doping concentration. In our LHOS NPs, Sm^{3+} ions occupy La^{3+} sites, and the matching charge does not invoke the need to compensate defects in the LHO lattice. This is an additional advantage of our LHOS NPs because such defects as nonradiative pathways are deleterious and adversely affect their performance.[55]

2.6. Colorimetric Performance of the LHOS NPs. As expected, the Commission Internationale de l'Eclairage (CIE) chromaticity diagram (Figure 3a) and the calculated CIE color coordinates (Table S4) demonstrate that the orange-red light emits from our LHOS NPs under 405 nm excitation because no PL spectral shift is seen as a function of Sm^{3+} doping concentration (Figure 2b). CCT is one of the important parameters to evaluate phosphor performance. It is reported that CCT values below 5000 K are ideal to generate artificial warm white light.[56] The CCT values of our LHOS NPs are calculated using McCamy and Kelly approximation mentioned in eq S5.[57,58]

The calculated CCT values of the LHOS NPs are in the range of 3057−3437 K (Table S4), and the variation of the CCT values is shown in Figure 3b. In that context, our LHOS NPs as red phosphors with CCT of 3266 K can be quite useful in designing a high-quality warm white light, which can be further explored for indoor and office lighting.[59] The CCT values reported for various europium- and samarium-doped inorganic oxides such as $GdPO_4$:Eu, $LiEu(WO_4)_2$, $CsGd(MoO_4)_2$:Eu, $LaPO_4$:Sm, and $GdPO_4$:Sm are 1704, 2175, 1627, 1984, and 1925 K, respectively.[60−63] In comparison to other lanthanide-doped inorganic oxides in terms of CCT, our LHOS-nanosized phosphors have an optimum value as a red phosphor.

2.7. Radioluminescence Performance of the LHOS NPs. Upon X-ray excitation, the LHOS NPs present four emission bands at 568, 611, 656, and 722 nm corresponding to $^4G_{5/2} \rightarrow {}^6H_{5/2}$, $^4G_{5/2} \rightarrow {}^6H_{7/2}$, $^4G_{5/2} \rightarrow {}^6H_{9/2}$, and $^4G_{5/2} \rightarrow {}^6H_{11/2}$ transitions of Sm^{3+} ions (Figure 4a). These radioluminescence (RL) spectra are obviously different from the corresponding PL spectra (Figure 2b). The RL asymmetry ratio was found to be 1.33 for the LHOS NPs (2.5%). The major difference is that the RL spectra show intense MDT $^4G_{5/2} \rightarrow {}^6H_{5/2}$ peak at 568 nm, which is absent in the PL spectra. This may be attributed to different mechanisms upon UV and X-ray excitations.

DOI: 10.1021/acsomega.9b01318
ACS Omega 2019, 4, 17956−17966

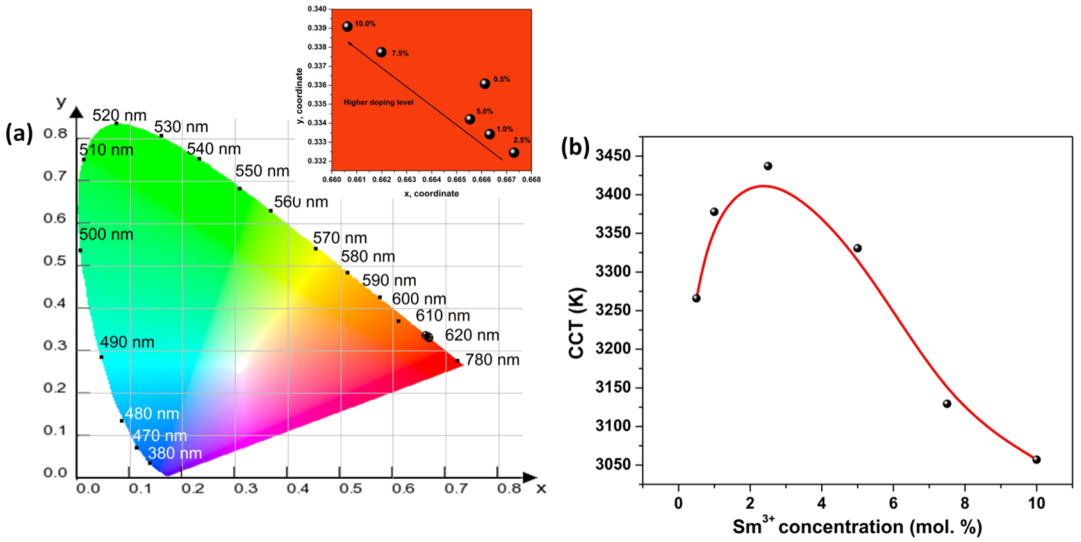

Figure 3. (a) CIE index diagram (excited at 405 nm) and (b) variation of the CCT with Sm^{3+} doping concentration of the LHOS NPs. The inset of Figure 3a shows the magnified color coordinates of the LHOS NPs with different Sm^{3+} concentrations.

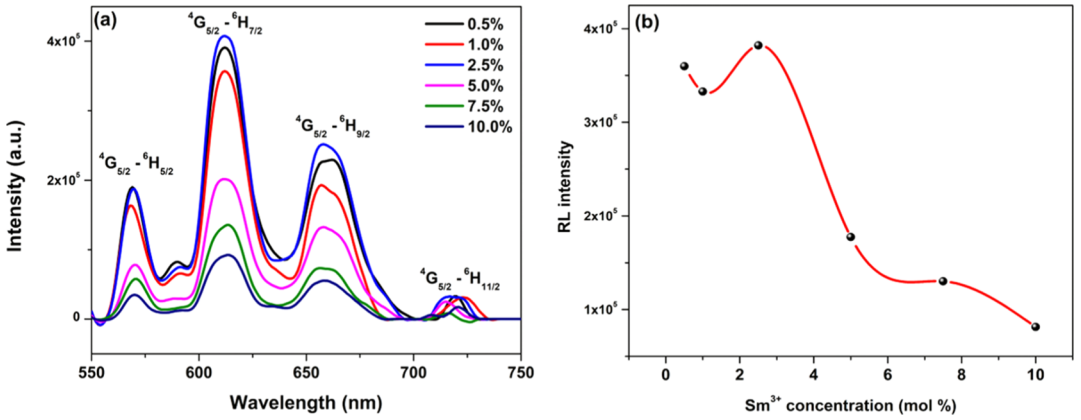

Figure 4. (a) RL emission spectra and (b) variation of RL emission intensity as a function of Sm^{3+} ion concentration of the LHOS NPs.

It is reported that lanthanide dopants are distributed at both La and Hf sites in multiple site lattices such as $La_2Hf_2O_7$.[38] LHO has ideal pyrochlore structure with distorted LaO_8 scalenohedra and perfect HfO_6 octahedra.[19] The EDT peak normally results when Sm^{3+} ions sitting at asymmetric La site is excited, whereas the MDT peak appears because of excitation of Sm ion sitting at symmetric Hf site. The luminescence processes under UV and X-ray irradiations are distinct because different mechanisms are involved. On X-ray irradiation, e^-−h^+ pairs are created because 4f−4f bands of Sm^{3+} ions and LHO are coexcited.[64] Under UV excitation, only the 4f−4f bands of Sm^{3+} ions are excited, but not the LHO host. Hence, in the LHOS NPs, a larger fraction of Sm^{3+} ions at the La site gets excited under UV excitation, leading to intense EDT and absence of MDT emission. On the other hand, both Sm^{3+} ions at La and Hf sites get excited under X-ray excitation, leading to both EDT and MDT emission peaks.

The nature of heavy constituents is very important for efficient X-ray scintillation process because X-ray absorption intensity varies proportionally to Z_{eff}^4/AE^3, where Z_{eff} and A are effective atomic number and atomic mass, respectively, and E is the energy of X-ray.[65] Accordingly, LHO is a desirable host for X-ray scintillators because of its high effective atomic number of Hf (72) and density (7.9 g/cc). In the first step, a scintillating material absorbs X-ray through photoelectric effect (PE), which creates electrons and holes. At the beginning, the X-ray (E < few 100 keV) interacts with Hf atom of the pyrochlore LHOS NPs mostly through PE. A similar interaction mechanism was predominant in $CsPbBr_3$ nanocrystals where X-ray interacts with the Pb atom of the perovskite nanocrystals through PE.[66]

As shown by the variation of integrated RL intensity between 575 and 675 nm corresponding to $^4G_{5/2} \rightarrow {}^6H_{7/2}$ as a function of Sm^{3+} concentration (Figure 4b), the maximum RL output is found to be with 2.5% Sm^{3+} doping concentration, which is similar to the PL results with quenching at higher concentrations. The emission intensity of phosphors is strongly affected by the surface defects present on nanostructured materials. There are two affecting parameters for luminescence properties: surface defects and agglomeration. Surface defects provide nonradiative pathways, whereas agglomeration scatters incident and emitted light. Hence, increasing these parameters reduces PL and RL intensities. Our SEM images show that there is a gradual decrease of particle size from 70 to 22 nm with increasing Sm^{3+} doping level from 0.5 to 10.0 mol % (Figure S3). The initial small decrease of the RL intensity with the increase of Sm^{3+} doping from 0.5 to 1.0% is within experimental error. The increase of RL intensity with the

DOI: 10.1021/acsomega.9b01318
ACS Omega 2019, 4, 17956−17966

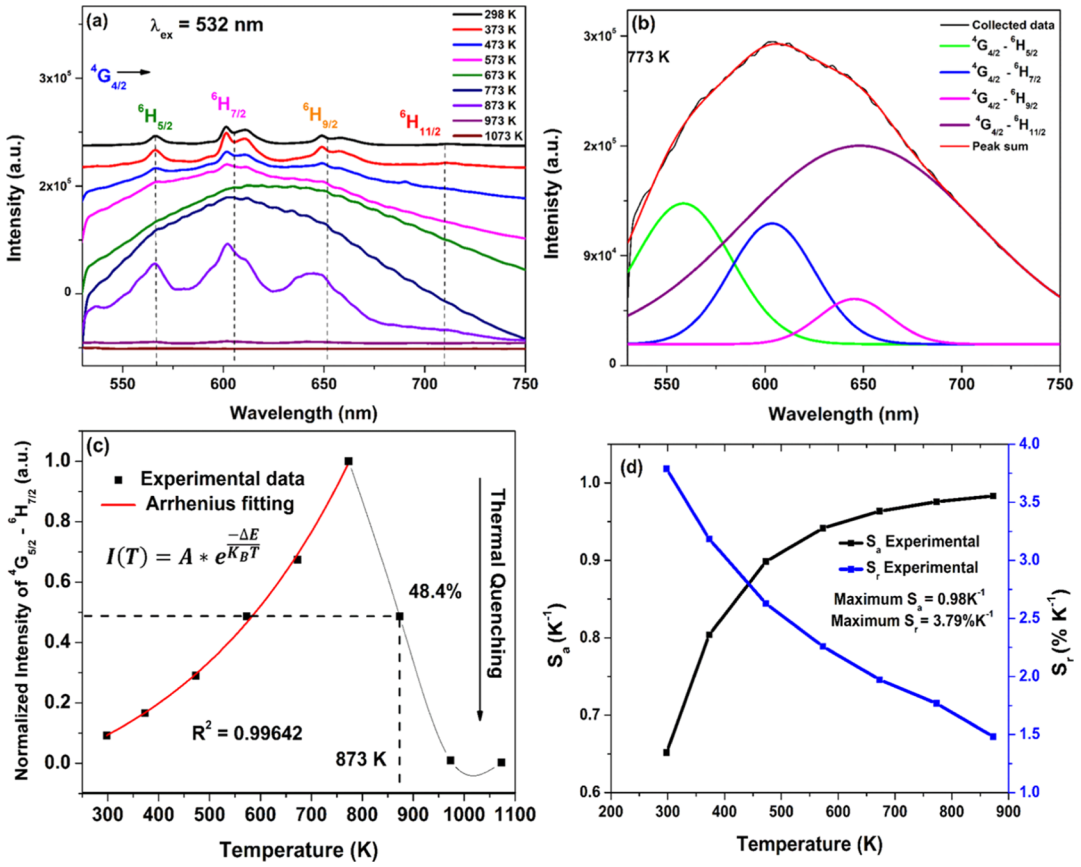

Figure 5. LHOS (2.5%) NPs: (a) in situ PL spectra measured from 298 to 1073 K. (b) Deconvoluted electronic transition peaks of Sm^{3+} ions at 773 K. (c) Arrhenius plot of the integrated PL intensity of $^4G_{5/2} \rightarrow {}^6H_{7/2}$ transition from 298 to 1073 K. (d) Variation of S_a and S_r as a function of temperature.

increase of Sm^{3+} doping from 1.0 to 2.5% is endowed by enhanced dopant concentration, which could overturn the negative effects by the decreased particle size and increased surface defect. When the Sm^{3+} doping level is higher than 2.5%, concentration quenching governs the observed RL trend.

2.8. Thermographic Performance of LHOS as a Phosphor. We have further investigated the thermal stability of the LHOS NPs and explored their potential application as TGPs by in situ PL measurements from 298 to 1073 K (Figure 5a). The LHOS (2.5%) NPs are used as an example because they possess the highest PL intensity. With increasing measurement temperature, the PL emission intensity initially increases and then decreases rather than monotonously decreases as normally seen from various doped phosphors.[38,40] Meanwhile, the well-resolved PL peaks pertaining to the Sm^{3+} ion broaden until 773 K (Figure 5b). The PL peaks are masked by broad envelope in the measurement temperature of 673−773 K, while the PL intensity is very weak between 973 and 1073 K. The broad envelope between 673 K up to 773 K may be attributed to large density of thermal defects (such as cation vacancies and cation interstitials) or oxygen vacancies, which can provide nonradiative pathways.[19,38,39] Another possible reason may be the partial reduction of Sm^{3+} to Sm^{2+} at high temperature, which is known to display a broad emission in the green region.[67] Techniques to probe defects in situ such as positron annihilation lifetime spectroscopy and to detect the Sm^{3+} to Sm^{2+} reduction in situ such as electron spin resonance spectroscopy would be helpful in this regard. Such an instrumental setup is not available to us, but we would try to seek collaborations in the future.

Of Sm^{3+}-doped phosphors, there are several nearly resonant cross-relaxation pathways which would not demonstrate temperature dependence.[68] The temperature-dependent change of PL emission intensity usually arises because the nonradiative transition probability of some particular energy levels is also temperature-dependent.[69] For our LHOS NPs, with the increase of PL measurement temperature, nonradiative transition probability reduces up to 773 K,[29,37] and therefore, the PL emission intensity increases in the temperature range of 298−773 K. However, at temperature higher than 773 K, there is a sudden thermal quench by ∼ 48% from 773 to 873 K (Figure 5c). This thermal quenching phenomenon occurs when phosphors are supersaturated with thermal heat and can no longer convert the excitation energy to visible light. Sudden and fast thermal quenching at high temperatures is typical of phosphors such as the LHOS NPs wherein nonresonant cross-relaxation channels (by about few hundred wavenumbers) become resonant at high temperature because of energy activation.[68]

We have extrapolated the activation energy value by Arrhenius fitting of the integrated PL intensity of $^4G_{5/2} \rightarrow {}^6H_{7/2}$ transition in the temperature range of 298−773 K based on eqs S6 and S7. The relationship of $\ln\left(\frac{I_o}{I} - 1\right)$ and $1/kT$ holds a linear fit (Figure S7) with a slope of −0.153, which is proportional to the involved activation energy of the LHOS-

DOI: 10.1021/acsomega.9b01318
ACS Omega 2019, 4, 17956−17966

2.5 NPs. Therefore, the activation energy is equal to 0.153 eV for the thermal quenching.

The absolute temperature sensitivity (S_a) is a vital parameter to quantitatively evaluate the optical thermometric ability of phosphors. S_a denotes the theoretical variation rate in fluorescence intensity ratio with respect to temperature and can be expressed by eq S8.

The absolute temperature sensitivity of our LHOS NPs increases with the increasing measurement temperature and reaches a maximum value of 0.98 K^{-1} (Figure 5d).

Meanwhile, relative temperature sensitivity (S_r) is another critical parameter to quantify the temperature sensing properties of thermometric materials. It is expressed by eq S9 as the relative change of the integrated PL intensity (I) with respect to temperature (T).

There is a gradual decrease of the S_r value with increasing measurement temperature for $^4G_{5/2} \rightarrow {}^6H_{7/2}$ transition of Sm^{3+} ions, which is similar to the trend observed from $GdVO_4$:Sm^{3+}(Figure 5d).[70] The S_r value from the LHOS NPs reaches a maximum of 3.79 % K^{-1}, which is the highest compared with typical temperature sensors (Table 1). The high activation energy and relatively good thermal sensitivity of synthesized LHOS NPs could be attributed to (a) low phonon energy of LHO, (b) high structural stability of LHO, and (c) little lattice strain or charge compensating defects as the majority of Sm^{3+} ions occupy La^{3+} sites because of similar ionic radii and the same charge.

Table 1. Relative Temperature Sensitivity S_r of Representative Optical Thermometric Materials

materials	maximum S_r (% K^{-1})	temperature range (K)	refs
Gd_2O_3:Er^{3+}/Yb^{3+}	0.39	300−900	71
$NaLuF_4$:Ho^{3+}/Yb^{3+}	0.12	350−750	72
$Yb_3Al_5O_{12}$:Er^{3+}	0.48	295−973	73
$NaLuF_4$:Gd^{3+}	0.29	298−523	74
Y_2MgTiO_6:Mn^{4+}	0.14	10−513	75
$GdVO_4$:Sm^{3+}	1.41	393−603	70
$La_2Hf_2O_7$:Sm^{3+}	3.79	298−873	this work

Thermographic and display panel applications of phosphors require them to possess high structural stability over a wide range of temperatures. Other than in situ PL measurements, we have also taken in situ XRD and Raman measurements on the LHOS (2.5%) NPs from 298 to 1148 and 1173 K, respectively (Figure S8). It is clearly seen that the LHOS NPs are structurally stable. High thermal stability of phosphors is favorable for luminescence thermometer application with high PL and RL efficiencies.

3. CONCLUSIONS

In summary, our LHOS NPs displayed strong orange-red emission with high color purity and low CCT under near-UV excitation at 405 nm, which makes them compatible with commercial NUV light-emitting diodes. The LHOS NPs are also applicable as an X-ray phosphor by converting highly energetic X-ray into orange-red light. Interestingly, their electronic and MDTs are different under UV and X-ray excitations. Meanwhile, the LHOS NPs demonstrate highest thermal sensitivity among typical temperature sensors. Therefore, the superior emission characteristics, efficient RL output, and good thermal sensing capability make the LHOS NPs potential candidates for multifunctional applications as phosphors, scintillators, and luminescence thermometry.

4. EXPERIMENTAL SECTION

4.1. Synthesis of the LHOS NPs. A set of six samples of LHO/x % Sm^{3+}, where x = 0.5, 1, 2.5, 5, 7.5, and 10, were prepared via a hybrid coprecipitation and MSS. Lanthanum nitrate hexahydrate ($La(NO_3)_3{\cdot}6H_2O$, 99.0%), hafnium dichloride oxide octahydrate ($HfCl_2O{\cdot}8H_2O$, 98%), and samarium nitrate ($Sm(NO_3)_3{\cdot}6H_2O$, 99.9%) were used as the starting reactants with no further purification. They were mixed and dissolved in distilled water (18.2 MΩ at 25 °C) together at an appropriate stoichiometric ratio and kept stirring for around 30 min. The solution was then titrated with 10% ammonium hydroxide solution (diluted from 28 to 30% NH_4OH) over a period of 2 h. The formed precipitate was then washed with deionized water, filtered, dried, and then mixed with potassium nitrate (KNO_3, 99.9%) and sodium nitrate ($NaNO_3$, 98%) in a stoichiometric ratio of (1:30:30). The mixture was finely grinded using a mortal and a pestle before being annealed at 650 °C for 6 h. The final resulting powder was washed and dried to obtain the final pure LHOS NPs. The schematic of the synthesis process employed for the LHOS NPs is depicted in Figure S1.

4.2. Characterization of the LHOS NPs. The XRD patterns were collected using a Rigaku MiniFlex X-ray diffractometer with a Cu Kα1 radiation (λ = 0.15406 nm, 30 kV, and 15 mA). The scanning mode used was 2θ, with a scanning range from 10° to 90° and a scanning step size of 0.05° with a scanning rate of 2° min^{-1}. FTIR spectra were collected using an FTIR ALPHA II's Platinum ATR single reflection diamond ATR module. Raman spectra were recorded on a Bruker SENTERRA Raman spectrometer (Bruker Optics SENTERRA R200) using a 785 nm laser with 100 mW power.

In situ Raman measurements were performed using a custom-built micro-Raman setup. The samples were placed in a high-temperature microscope stage (TS-1500, Linkam) and were excited with a continuous wave diode-pumped solid-state laser (Excelsior, Spectra Physics, 532 nm) through an upright microscope using a 50× long-working distance objective with NA (numeric aperture) = 0.5. The typical incident laser power on a sample was maintained at ∼100 μW. The scattered Raman light was analyzed by a spectrometer (SpectraPro 2300i, Acton, f = 0.3 m) that was coupled to the microscope and equipped with a 1800 grooves/mm grating and a CCD camera (Pixis 256BR, Princeton Instruments).

The optical properties of the NPs were evaluated using an Edinburgh Instrument FLS 980 fluorometer system equipped with both a steady-state and a pulsed Xe lamp source. The Xe-pulsed source has a frequency range of 1−100 Hz. RL spectra were acquired with a silver target as the X-ray source with λ = 0.52 Å at a power of 12 W (60 kV and 200 μA). The silver target was adapted to the Edinburgh Instruments FLS 980 fluorimeter system. No filters were used during the process. Lead shielding was used to block the incoming radiation lower than 2 mR/h.

■ ASSOCIATED CONTENT

Supporting Information

The Supporting Information is available free of charge on the ACS Publications website at DOI: 10.1021/acsomega.9b01318.

DOI: 10.1021/acsomega.9b01318
ACS Omega 2019, 4, 17956−17966

Materials synthesis and instrumentation: XRD, Raman spectroscopy, FTIR spectroscopy, in situ XRD and Raman, and SEM; MSS of the LHOS NPs, XRD patterns, Raman spectra, FTIR spectra, in situ XRD and Raman spectra, and SEM; and crystallite size, concentration quenching values, color coordinates, CCT, and excited-state lifetimes (PDF)

AUTHOR INFORMATION

Corresponding Author

*E-mail: ymao17@iit.edu, yuanbing.mao@utrgv.edu. Phone: +1-312-567-3815, +1 956 665 2986, Fax: +1 956 665 5006.

ORCID

Santosh K. Gupta: 0000-0002-1178-0159

Alexander A. Puretzky: 0000-0002-9996-4429

Yuanbing Mao: 0000-0003-2665-6676

Present Address

⊥Department of Chemistry, Illinois Institute of Technology, 3105 South Dearborn Street, Chicago, Illinois 60616, United States.

Notes

The authors declare no competing financial interest.

ACKNOWLEDGMENTS

The authors thank the financial support by the National Science Foundation under CHE (award #1710160). S.K.G. thanks the United States−India Education Foundation (USIEF, India) and the Institute of International Education (IIE, USA) for his Fulbright Nehru Postdoctoral Fellowship (Award no. 2268/FNPDR/2017). In situ Raman and PL measurements were conducted at the Center for Nanophase Materials Sciences, which is a DOE Office of Science User Facility.

REFERENCES

(1) Shang, X.; Song, I.; Jung, G. Y.; Choi, W.; Ohtsu, H.; Lee, J. H.; Koo, J. Y.; Liu, B.; Ahn, J.; Kawano, M.; Kwak, S. K.; Oh, J. H. Chiral self-sorted multifunctional supramolecular biocoordination polymers and their applications in sensors. *Nat. Commun.* **2018**, *9*, 3933.

(2) Meng, C.; Muralidharan, N.; Teblum, E.; Moyer, K. E.; Nessim, G. D.; Pint, C. L. Multifunctional Structural Ultrabattery Composite. *Nano Lett.* **2018**, *18*, 7761−7768.

(3) Zhang, C.; Wu, W.; Li, R. Q.; Qiu, W. X.; Zhuang, Z. N.; Cheng, S. X.; Zhang, X. Z. Peptide-Based Multifunctional Nanomaterials for Tumor Imaging and Therapy. *Adv. Funct. Mater.* **2018**, *28*, 1804492.

(4) Chen, S.; Zhang, N.; Zhang, B.; Zhang, B.; Song, J. Multifunctional Self-Healing Ionogels from Supramolecular Assembly: Smart Conductive and Remarkable Lubricating Materials. *ACS Appl. Mater. Interfaces* **2018**, *10*, 44706−44715.

(5) Du, A.; Wang, H.; Zhou, B.; Zhang, C.; Wu, X.; Ge, Y.; Niu, T.; Ji, X.; Zhang, T.; Zhang, Z.; Wu, G.; Shen, J. Multifunctional Silica Nanotube Aerogels Inspired by Polar Bear Hair for Light Management and Thermal Insulation. *Chem. Mater.* **2018**, *30*, 6849−6857.

(6) Kim, D.; Shin, K.; Kwon, S. G.; Hyeon, T. Synthesis and Biomedical Applications of Multifunctional Nanoparticles. *Adv. Mater.* **2018**, *30*, 1802309.

(7) Rabouw, F. T.; Prins, P. T.; Villanueva-Delgado, P.; Castelijns, M.; Geitenbeek, R. G.; Meijerink, A. Quenching Pathways in $NaYF_4$:Er^{3+},Yb^{3+} Upconversion Nanocrystals. *ACS Nano* **2018**, *12*, 4812−4823.

(8) Panigrahi, K.; Saha, S.; Sain, S.; Chatterjee, R.; Das, A.; Ghorai, U. K.; Sankar Das, N.; Chattopadhyay, K. K. White light emitting $MgAl_2O_4$:Dy^{3+},Eu^{3+} nanophosphor for multifunctional applications. *Dalton Trans.* **2018**, *47*, 12228−12242.

(9) Kim, J.; Michelin, S.; Hilbers, M.; Martinelli, L.; Chaudan, E.; Amselem, G.; Fradet, E.; Boilot, J.-P.; Brouwer, A. M.; Baroud, C. N.; Peretti, J.; Gacoin, T. Monitoring the orientation of rare-earth-doped nanorods for flow shear tomography. *Nat. Nanotechnol.* **2017**, *12*, 914.

(10) Bünzli, J.-C. G.; Piguet, C. Taking advantage of luminescent lanthanide ions. *Chem. Soc. Rev.* **2005**, *34*, 1048−1077.

(11) Eliseeva, S. V.; Bünzli, J.-C. G. Lanthanide luminescence for functional materials and bio-sciences. *Chem. Soc. Rev.* **2010**, *39*, 189−227.

(12) Liao, S.; Ji, X.; Liu, Y.; Zhang, J. Highly Efficient and Thermally Stable Blue-Green $(Ba_{0.8}Eu_{0.2}O)(Al_2O_3)_{4.575\times(1+x)}$ Phosphor through Structural Modification. *ACS Appl. Mater. Interfaces* **2018**, *10*, 39064−39073.

(13) Jacoby, M. The chemical search for better white light *Chem. Eng. News.* 2018, *96*, 46, https://cen.acs.org/materials/inorganic-chemistry/chemical-search-better-white-light/96/i46.

(14) Pust, P.; Weiler, V.; Hecht, C.; Tücks, A.; Wochnik, A. S.; Henß, A.-K.; Wiechert, D.; Scheu, C.; Schmidt, P. J.; Schnick, W. Narrow-band red-emitting $Sr[LiAl_3N_4]$:Eu^{2+} as a next-generation LED-phosphor material. *Nat. Mater.* **2014**, *13*, 891.

(15) Jung, J. Y.; Hirata, G. A.; Gundiah, G.; Derenzo, S.; Wrasidlo, W.; Kesari, S.; Makale, M. T.; McKittrick, J. Identification and development of nanoscintillators for biotechnology applications. *J. Lumin.* **2014**, *154*, 569−577.

(16) Klein, J. S.; Sun, C.; Pratx, G. Radioluminescence in biomedicine: physics, applications, and models. *Phys. Med. Biol.* **2019**, *64*, 04TR01.

(17) Wang, X.; Liu, Q.; Bu, Y.; Liu, C.-S.; Liu, T.; Yan, X. Optical temperature sensing of rare-earth ion doped phosphors. *RSC Adv.* **2015**, *5*, 86219−86236.

(18) Đačanin Far, L.; Lukić-Petrović, S. R.; Đorđević, V.; Vuković, K.; Glais, E.; Viana, B.; Dramićanin, M. D. Luminescence temperature sensing in visible and NIR spectral range using Dy^{3+} and Nd^{3+} doped $YNbO_4$. *Sens. Actuators, A* **2018**, *270*, 89−96.

(19) Gupta, S. K.; Zuniga, J. P.; Abdou, M.; Mao, Y. Thermal annealing effects on $La_2Hf_2O_7$:Eu^{3+} nanoparticles: a curious case study of structural evolution and site-specific photo- and radioluminescence. *Inorg. Chem. Front.* **2018**, *5*, 2508−2521.

(20) Ting, C.-C.; Chiu, Y.-S.; Chang, C.-W.; Chuang, L.-C. Visible and infrared luminescence properties of Er^{3+}-doped $Y_2Ti_2O_7$ nanocrystals. *J. Solid State Chem.* **2011**, *184*, 563−571.

(21) Dixie, L. C. Samarium doped alkaline earth halides as red-emitting scintillators and phosphors. Ph.D. Thesis, Victoria University of Wellington, 2013.

(22) Sayed, F. N.; Grover, V.; Bhattacharyya, K.; Jain, D.; Arya, A.; Pillai, C. G. S.; Tyagi, A. K. $Sm_{2-x}Dy_xZr_2O_7$ pyrochlores: probing order− disorder dynamics and multifunctionality. *Inorg. Chem.* **2011**, *50*, 2354−2365.

(23) Turner, K. M.; Rittman, D. R.; Heymach, R. A.; Tracy, C. L.; Turner, M. L.; Fuentes, A. F.; Mao, W. L.; Ewing, R. C. Pressure-induced structural modifications of rare-earth hafnate pyrochlore. *J. Phys.: Condens. Matter* **2017**, *29*, 255401.

(24) Subramanian, M. A.; Aravamudan, G.; Subba Rao, G. V. Oxide pyrochlores—a review. *Prog.Solid Sate Chem.* **1983**, *15*, 55−143.

(25) Zuniga, J. P.; Gupta, S. K.; Abdou, M.; Mao, Y. Effect of molten salt synthesis processing duration on the photo- and radioluminescence of UV-, Visible-, and X-ray-excitable $La_2Hf_2O_7$:Eu^{3+} nanoparticles. *ACS Omega* **2018**, *3*, 7757−7770.

(26) Pokhrel, M.; Gupta, S. K.; Wahid, K.; Mao, Y. Pyrochlore Rare-Earth Hafnate $RE_2Hf_2O_7$ (RE = La and Pr) Nanoparticles Stabilized by Molten-Salt Synthesis at Low Temperature. *Inorg. Chem.* **2019**, *58*, 1241.

(27) Garg, N.; Pandey, K. K.; Murli, C.; Shanavas, K. V.; Mandal, B. P.; Tyagi, A. K.; Sharma, S. M. Decomposition of lanthanum hafnate at high pressures. *Phys. Rev. B: Condens. Matter Mater. Phys.* **2008**, *77*, 214105.

(28) Zinatloo-Ajabshir, S.; Salavati-Niasari, M. Facile synthesis of nanocrystalline neodymium zirconate for highly efficient photodegradation of organic dyes. *J. Mol. Liq.* **2017**, *243*, 219−226.

DOI: 10.1021/acsomega.9b01318
ACS Omega 2019, 4, 17956−17966

(29) Gupta, S. K.; Zuniga, J. P.; Abdou, M.; Mao, Y. Thermal annealing effects on $La_2Hf_2O_7:Eu^{3+}$ nanoparticles: a curious case study of structural evolution and site-specific photo- and radioluminescence. *Inorg. Chem. Front.* **2018**, *5*, 2508−2521.
(30) Sevastyanov, V. G.; Simonenko, E. P.; Simonenko, N. P.; Stolyarova, V. L.; Lopatin, S. I.; Kuznetsov, N. T. Synthesis, vaporization and thermodynamic properties of superfine $Nd_2Hf_2O_7$ and $Gd_2Hf_2O_7$. *Eur. J. Inorg. Chem.* **2013**, *2013*, 4636−4644.
(31) Klee, W. E.; Weitz, G. Infrared spectra of ordered and disordered pyrochlore-type compounds in the series $RE_2Ti_2O_7$, $RE_2Zr_2O_7$ and $RE_2Hf_2O_7$. *J. Inorg. Nucl. Chem.* **1969**, *31*, 2367−2372.
(32) Chen, B. J.; Shen, L. F.; Pun, E. Y. B.; Lin, H. Sm^{3+}-doped germanate glass channel waveguide as light source for minimally invasive photodynamic therapy surgery. *Opt. Express* **2012**, *20*, 879−889.
(33) Gupta, S. K.; Ghosh, P. S.; Pathak, N.; Arya, A.; Natarajan, V. Understanding the local environment of Sm^{3+} in doped $SrZrO_3$ and energy transfer mechanism using time-resolved luminescence: a combined theoretical and experimental approach. *RSC Adv.* **2014**, *4*, 29202−29215.
(34) Garbout, A.; Férid, M. Pyrochlore structure and spectroscopic studies of titanate ceramics. A comparative investigation on $SmDyTi_2O_7$ and $YDyTi_2O_7$ solid solutions. *Spectrochim. Acta, Part A* **2018**, *198*, 188−197.
(35) Gupta, S. K.; Pathak, N.; Sahu, M.; Natarajan, V. A Novel near white light emitting nanocrystalline $Zn_2P_2O_7:Sm^{3+}$ derived using citrate precursor route: Photoluminescence spectroscopy. *Adv. Powder Technol.* **2014**, *25*, 1388−1393.
(36) Seguini, G.; Spiga, S.; Bonera, E.; Fanciulli, M.; Reyes Huamantinco, A.; Först, C. J.; Ashman, C. R.; Blöchl, P. E.; Dimoulas, A.; Mavrou, G. Band alignment at the $La_2Hf_2O_7/(001)Si$ interface. *Appl. Phys. Lett.* **2006**, *88*, 202903.
(37) Gupta, S. K.; Sudarshan, K.; Ghosh, P. S.; Srivastava, A. P.; Bevara, S.; Pujari, P. K.; Kadam, R. M. Role of various defects in the photoluminescence characteristics of nanocrystalline $Nd_2Zr_2O_7$: an investigation through spectroscopic and DFT calculations. *J. Mater. Chem. C* **2016**, *4*, 4988−5000.
(38) Gupta, S. K.; Zuniga, J. P.; Ghosh, P. S.; Abdou, M.; Mao, Y. Correlating Structure and Luminescence Properties of Undoped and Eu^{3+}-Doped $La_2Hf_2O_7$ Nanoparticles Prepared with Different Coprecipitating pH Values through Experimental and Theoretical Studies. *Inorg. Chem.* **2018**, *57*, 11815−11830.
(39) Qin, X.; Liu, X.; Huang, W.; Bettinelli, M.; Liu, X. Lanthanide-Activated Phosphors Based on 4f-5d Optical Transitions: Theoretical and Experimental Aspects. *Chem. Rev.* **2017**, *117*, 4488−4527.
(40) Gupta, S. K.; Abdou, M.; Ghosh, P. S.; Zuniga, J. P.; Mao, Y. Thermally Induced Disorder−Order Phase Transition of $Gd_2Hf_2O_7:Eu^{3+}$ Nanoparticles and Its Implication on Photo- and Radioluminescence. *ACS Omega* **2019**, *4*, 2779−2791.
(41) Dexter, D. L. A Theory of Sensitized Luminescence in Solids. *J. Chem. Phys.* **1953**, *21*, 836−850.
(42) Maheshwary, M.; Singh, B. P.; Singh, R. A. Color tuning in thermally stable Sm^{3+}-activated $CaWO_4$ nanophosphors. *New J. Chem.* **2015**, *39*, 4494−4507.
(43) Blasse, G. Energy transfer between inequivalent Eu^{2+} ions. *J. Solid State Chem.* **1986**, *62*, 207−211.
(44) Gupta, S. K.; Reghukumar, C.; Kadam, R. M. Eu^{3+} local site analysis and emission characteristics of novel $Nd_2Zr_2O_7$:Eu phosphor: insight into the effect of europium concentration on its photoluminescence properties. *RSC Adv.* **2016**, *6*, 53614−53624.
(45) Gupta, S. K.; Reghukumar, C.; Sudarshan, K.; Ghosh, P. S.; Pathak, N.; Kadam, R. M. Orange-red emitting $Gd_2Zr_2O_7:Sm^{3+}$: Structure-property correlation, optical properties and defect spectroscopy. *J. Phys. Chem. Solids* **2018**, *116*, 360−366.
(46) Mohapatra, M.; Rajeswari, B.; Hon, N. S.; Kadam, R. M.; Natarajan, V. Photoluminescence properties of 'red' emitting $La_2Zr_2O_7$:Eu pyrochlore ceramics for potential phosphor application. *J. Lumin.* **2015**, *166*, 1−7.
(47) Bayart, A.; Szczepanski, F.; Blach, J.-F.; Rousseau, J.; Katelnikovas, A.; Saitzek, S. Upconversion luminescence properties and thermal quenching mechanisms in the layered perovskite $La_{1.9}Er_{0.1}Ti_2O_7$ towards an application as optical temperature sensor. *J. Alloys Compd.* **2018**, *744*, 516−527.
(48) Dai, P.; Zhang, X.; Zhou, M.; Li, X.; Yang, J.; Sun, P.; Xu, C.; Liu, Y. Thermally Stable Pyrochlore $Y_2Ti_2O_7:Eu^{3+}$ Orange−Red Emitting Phosphors. *J. Am. Ceram. Soc.* **2012**, *95*, 658−662.
(49) Tiwari, H.; Varadaraju, U. V.; Naidu, S. A. Eu^{3+} Photoluminescence in $CaYTiNbO_7$ Pyrochlore: A Promising Orange-Red Phosphor for White-Light-Emitting Diodes. *ChemistrySelect* **2017**, *2*, 10741−10747.
(50) Van Uitert, L. G. Characterization of energy transfer interactions between rare earth ions. *J. Electrochem. Soc.* **1967**, *114*, 1048−1053.
(51) Gupta, S. K.; Zuniga, J. P.; Abdou, M.; Thomas, M.; De Alwis Goonatilleke, M.; Guiton, B. S.; Mao, Y. Lanthanide-doped lanthanum hafnate nanoparticles as multicolor phosphors for warm white lighting and scintillators. *Chem. Eng. J.* **2020**, *379*, 122314.
(52) Zhong, J.; Chen, D.; Zhou, Y.; Wan, Z.; Ding, M.; Ji, Z. Stable and chromaticity-tunable phosphor-in-glass inorganic color converter for high-power warm white light-emitting diode. *J. Eur. Ceram. Soc.* **2016**, *36*, 1705−1713.
(53) Shukla, R.; Gupta, S. K.; Yadav, H.; Ranjane, P.; Kadam, R. M.; Achary, S. N.; Tyagi, A. K. A carnegieite type red emitting $NaAlSiO_4:Eu^{3+}$ phosphor: Concentration dependent time resolved photoluminescence and Judd-Ofelt analysis. *J. Lumin.* **2019**, *209*, 283−290.
(54) Gupta, S. K.; Mohapatra, M.; Natarajan, V.; Godbole, S. V. Site-specific luminescence of Eu^{3+} in gel-combustion-derived strontium zirconate perovskite nanophosphors. *J. Mater. Sci.* **2012**, *47*, 3504−3515.
(55) Gupta, S. K.; Sudarshan, K.; Yadav, A. K.; Gupta, R.; Bhattacharyya, D.; Jha, S. N.; Kadam, R. M. Deciphering the Role of Charge Compensator in Optical Properties of $SrWO_4:Eu^{3+}$: A (A= Li^+, Na^+, K^+): Spectroscopic Insight Using Photoluminescence, Positron Annihilation, and X-ray Absorption. *Inorg. Chem.* **2018**, *57*, 821−832.
(56) Pratapkumar, C.; Prashantha, S. C.; Nagabhushana, H.; Jnaneshwara, D. M. Photoluminescence and photometric studies of low temperature prepared red emitting $MgAl_2O_4:Cr^{3+}$ nanophosphors for solid state displays. *J. Sci. Adv. Mater. Devices* **2018**, *3*, 464−470.
(57) McCamy, C. S. Correlated color temperature as an explicit function of chromaticity coordinates. *Color Res. Appl.* **1992**, *17*, 142−144.
(58) Kelly, K. L. Lines of Constant Correlated Color Temperature Based on MacAdam's (u,υ) Uniform Chromaticity Transformation of the CIE Diagram. *J. Opt. Soc. Am.* **1963**, *53*, 999−1002.
(59) Li, P.; Wang, Z.; Yang, Z.; Guo, Q. A novel, warm, white light-emitting phosphor $Ca_2PO_4Cl:Eu^{2+},Mn^{2+}$ for white LEDs. *J. Mater. Chem. C* **2014**, *2*, 7823−7829.
(60) Devakumar, B.; Halappa, P.; Shivakumara, C. Dy^{3+}/Eu^{3+} co-doped $CsGd(MoO_4)_2$ phosphor with tunable photoluminescence properties for near-UV WLEDs applications. *Dyes Pigm.* **2017**, *137*, 244−255.
(61) Wang, H.; Li, Y.; Ning, Z.; Huang, L.; Zhong, C.; Wang, C.; Liu, M.; Lai, X.; Gao, D.; Bi, J. A novel red phosphor $Li_xNa_{1-x}Eu(WO_4)_2$ solid solution: Influences of Li/Na ratio on the microstructures and luminescence propertiesr. *J. Lumin.* **2018**, *201*, 364−371.
(62) Mathur, A.; Halappa, P.; Shivakumara, C. Synthesis and characterization of Sm^{3+} activated $La_{1-x}Gd_xPO_4$ phosphors for white LEDs applications. *J. Mater. Sci.: Mater. Electron.* **2018**, *29*, 19951−19964.
(63) Halappa, P.; Devakumar, B.; Shivakumara, C. Effect of Ca^{2+} ion co-doping on radiative properties via tuning the local symmetry around the Eu^{3+} ions in orange red light emitting $GdPO_4:Eu^{3+}$ phosphors. *New J. Chem.* **2019**, *43*, 63−71.

DOI: 10.1021/acsomega.9b01318
ACS Omega 2019, 4, 17956−17966

(64) Zuniga, J. P.; Gupta, S. K.; Pokhrel, M.; Mao, Y. Exploring the optical properties of $La_2Hf_2O_7$:Pr^{3+} nanoparticles under UV and X-ray excitation for potential lighting and scintillating applications. *New J. Chem.* **2018**, *42*, 9381−9392.
(65) Nikl, M.; Yoshikawa, A. Recent R&D Trends in Inorganic Single-Crystal Scintillator Materials for Radiation Detection. *Adv. Opt. Mater.* **2015**, *3*, 463−481.
(66) Chen, Q.; Wu, J.; Ou, X.; Huang, B.; Almutlaq, J.; Zhumekenov, A. A.; Guan, X.; Han, S.; Liang, L.; Yi, Z.; Li, J.; Xie, X.; Wang, Y.; Li, Y.; Fan, D.; Teh, D. B. L.; All, A. H.; Mohammed, O. F.; Bakr, O. M.; Wu, T.; Bettinelli, M.; Yang, H.; Huang, W.; Liu, X. All-inorganic perovskite nanocrystal scintillators. *Nature* **2018**, *561*, 88−93.
(67) Huang, Y.; Zhao, W.; Shi, L.; Seo, H. J. Structural defects and luminescence properties of Sm^{2+} ions doped in $BaBPO_5$ phosphor by X-ray irradiation. *J. Alloys Compd.* **2009**, *477*, 936−940.
(68) Kaczkan, M.; Boruc, Z.; Turczyński, S.; Malinowski, M. Effect of temperature on the luminescence of Sm^{3+} ions in YAM crystals. *J. Alloys Compd.* **2014**, *612*, 149−153.
(69) Wade, S. A.; Collins, S. F.; Baxter, G. W. Fluorescence intensity ratio technique for optical fiber point temperature sensing. *J. Appl. Phys.* **2003**, *94*, 4743−4756.
(70) Cai, J.; Zhao, L.; Hu, F.; Wei, X.; Chen, Y.; Yin, M.; Duan, C.-K. Temperature sensing using thermal population of low-lying energy levels with $(Sm_{0.01}Gd_{0.99})VO_4$. *Inorg. Chem.* **2017**, *56*, 4039−4046.
(71) Singh, S. K.; Kumar, K.; Rai, S. B. Er^{3+}/Yb^{3+} codoped Gd_2O_3 nano-phosphor for optical thermometry. *Sens. Actuators, A* **2009**, *149*, 16−20.
(72) Zhou, S.; Jiang, S.; Wei, X.; Chen, Y.; Duan, C.; Yin, M. Optical thermometry based on upconversion luminescence in Yb^{3+}/Ho^{3+} co-doped $NaLuF_4$. *J. Alloys Compd.* **2014**, *588*, 654−657.
(73) Dong, B.; Cao, B.; He, Y.; Liu, Z.; Li, Z.; Feng, Z. Temperature Sensing and In Vivo Imaging by Molybdenum Sensitized Visible Upconversion Luminescence of Rare-Earth Oxides. *Adv. Mater.* **2012**, *24*, 1987−1993.
(74) Zheng, K.; Liu, Z.; Lv, C.; Qin, W. Temperature sensor based on the UV upconversion luminescence of Gd^{3+} in $Yb^{3+}-Tm^{3+}-Gd^{3+}$ codoped $NaLuF_4$ microcrystals. *J. Mater. Chem. C* **2013**, *1*, 5502−5507.
(75) Cai, P.; Qin, L.; Chen, C.; Wang, J.; Bi, S.; Kim, S. I.; Huang, Y.; Seo, H. J. Optical Thermometry Based on Vibration Sidebands in Y_2MgTiO_6:Mn^{4+} Double Perovskite. *Inorg. Chem.* **2018**, *57*, 3073−3081.

DOI: 10.1021/acsomega.9b01318
ACS Omega 2019, 4, 17956−17966